Journal of Groundwater Science and Engineering
ISSN 2305-7068
Indexed by ESCI CABI CSA
Scopus GeoRef AJ CNKI

Comparative evaluation of upscaled analytical and numerical models for DNAPL dissolution processes

Pan-rui Yang, Xiao-min Yuan, Hui-rong Guo, Bao-lan Li, Xing-quan Wang, Min Yuan

Citation:
Yang PR, Yuan XM, Guo HR, Li BL, Wang XQ, Yuan M. 2026. Comparative evaluation of upscaled analytical and numerical models for DNAPL dissolution processes. Journal of Groundwater Science and Engineering, 14(3): 382-398.

View online: https://doi.org/10.26599/JGSE.2026.9280088

Articles you may be interested in

Analytical solution for Non-Darcian effect on transient confined-unconfined flow in a confined aquifer
Journal of Groundwater Science and Engineering. 2023, 11(4): 365-378 https://doi.org/10.26599/JGSE.2023.9280029

Analytical solutions for constant-rate test in bounded confined aquifers with non-Darcian effect
Journal of Groundwater Science and Engineering. 2022, 10(4): 311-321 https://doi.org/10.19637/j.cnki.2305-7068.2022.04.001

Holistic approach of GIS based Multi-Criteria Decision Analysis (MCDA) and WetSpass models to evaluate groundwater potential in Gelana watershed of Ethiopia
Journal of Groundwater Science and Engineering. 2022, 10(2): 138-152 https://doi.org/10.19637/j.cnki.2305-7068.2022.02.004

A state-of-the-art Fuzzy Nonlinear Additive Regression (FNAR) model for groundwater level prediction
Journal of Groundwater Science and Engineering. 2026, 14(1): 83-99 https://doi.org/10.26599/JGSE.2026.9280074

Web-based tool for analyzing the seawater-freshwater interface using analytical solutions and SEAWAT code comparison
Journal of Groundwater Science and Engineering. 2025, 13(3): 250-267 https://doi.org/10.26599/JGSE.2025.9280053

Evaluation of groundwater resource potential by using water balance model: A case of Upper Gilgel Gibe Watershed, Ethiopia
Journal of Groundwater Science and Engineering. 2022, 10(3): 209-222 https://doi.org/10.19637/j.cnki.2305-7068.2022.03.001

Journal of Groundwater Science and Engineering 14(2026) 382–398

Journal homepage: http://gwse.iheg.org.cn

Research Article

Comparative evaluation of upscaled analytical and numerical models for DNAPL dissolution processes

Pan-rui Yang[1,2], Xiao-min Yuan[1,2], Hui-rong Guo[3*], Bao-lan Li[1,2], Xing-quan Wang[1,2], Min Yuan[3]

[1] *School of Ecology and Environmental Science*, *Qinghai Institute of Technology*, *Xining* 810016, *China*.
[2] *Qinghai Provincial Key Laboratory of Plateau Climate Change and Corresponding Ecological and Environmental Effects*, *Xining* 810016, *China*.
[3] *School of Environmental Studies*, *China University of Geosciences*, *Wuhan* 430074, *China*.

Abstract: Mathematical model-based accurate evaluation of the remediation process at organic pollution sites serves as an efficient approach to the management and remediation of contaminant source zones. Numerical and upscaled analytical solution models are effective mathematical methods for reproducing the Dense Nonaqueous Phase Liquid (DNAPL) remediation process. However, in the current design of pollutant removal schemes, effective mass transfer models for characterizing the elution behaviors of contaminants remain lacking. In this study, two mathematical methods integrated with improved mass transfer models were employed to simulate the multi-stage contaminant elution behaviors under two distinct scenarios: A mixed-source region subjected to continuous water flushing and a residual DNAPL source treated with shorter-duration pulse flushing of the ethanol solution. Both the improved numerical model and upscaled analytical solution model demonstrated enhanced accuracy, which was attributed to the incorporation of solubilization mechanisms into mass transfer processes and the adoption of a multi-source region division method. The Mean Absolute Errors (MAE) of the numerical simulation for the two scenarios were 20.68 mg/L and 6.93 mg/L, respectively, whereas those of the upscaled model were 33.29 mg/L and 8.60 mg/L, respectively. Comparing the two improved models, the numerical model exhibited higher accuracy, while the upscaled model was characterized by faster computation speed and fewer input parameters.

Keywords: Mass transfer rate coefficient; Numerical model; Analytical solution model; Multi-stage dissolution behaviors

Received: 05 Aug 2025/ Accepted: 28 Mar 2026/ Published: 30 Jul 2026

Introduction

The improper production and use of organic solvents and hydrocarbon fuels, coupled with their leakage into the underground environment, have gradually developed into a persistent pollution source that threatens the safety of groundwater utilization over extended periods (Huo et al., 2020). It remains a major challenge to effectively remove these organic pollutants from the underground environment in the environmental engineering field (Feng et al., 2025; Oba et al., 2021; Zhao et al., 2024). Many studies have been conducted on the dissolution and removal of Dense Nonaqueous Phase Liquid (DNAPL) to understand the mechanisms of DNAPL remediation over the past several decades (Patil et al., 2023, Tiwari and Tripathy, 2023). Mass transfer serves as a key factor in controlling the DNAPL dissolution process. Due to the heterogeneity of soil media and DNAPL distributions, as well as the complexities in most field applications, a mass transfer rate expression is necessary for describing the simulation of DNAPL dissolution process (Agaoglu et al.,

*Corresponding author: Hui-rong Guo, *E-mail address*: elsieguo@126.com

DOI: 10.26599/JGSE.2026.9280088

Yang PR, Yuan XM, Guo HR, et al. 2026. Comparative evaluation of upscaled analytical and numerical models for DNAPL dissolution processes. Journal of Groundwater Science and Engineering, 14(3): 382-398.

2305-7068/© 2026 Journal of Groundwater Science and Engineering Editorial Office This is an open access article under the CC BY-NC-ND license (http://creativecommons.org/licenses/by-nc-nd/4.0)

2012; Grant and Gerhard, 2007).

Factors affecting the mass transfer rate include pore velocities of flushing solutions, the DNAPL dissolution capacity in flushing solutions, pore characteristics, and the interfacial area between two phases in pores, according to a series of pore-scale mass transfer experiments (Corapcioglu et al., 2009; Hu et al., 2021; Ramezanzadeh et al., 2020; Sarikurt et al., 2017; Wang et al., 2023a; Yang et al., 2022). Several mass transfer models have been established based on previous studies. Although several experimental investigations have been conducted to characterize the effects of DNAPL solubility on associated mass transfer processes, the quantitative relationships between them have not yet been fully clarified (Cho et al., 2005; Ramezanzadeh et al., 2020; Yuan et al., 2025).

In some studies, it has been shown that DNAPL solubilization inhibits DNAPL mass transfer (Wang et al., 2023a, b; Yaksi et al., 2020). There was also the investigation indicating that solubilization could enhance DNAPL mass transfer (Yang et al., 2022). In addition, several new mass transfer models were developed to characterize the mass transfer process in complex DNAPL source zone configurations. These models incorporated macroscopic DNAPL distribution characteristics, including the GTP (the ganglia-to-pool ratio), as well as the perimeter and area of the DNAPL source region (Luciano et al., 2018; Saba and Illangasekare, 2000).

DNAPL remediation simulations can predict the multi-stage behavior of effluent concentrations when these macroscopic DNAPL source parameters are considered. As the mass transfer rate in a DNAPL pool region is significantly lower than that in the ganglia region, it is essential to evaluate mass transfer rates separately for these distinct DNAPL configurations (Christ et al., 2010; Guo et al., 2020; Stewart et al., 2022).

Due to the high uncertainty and complexity in mathematical descriptions of DNAPL multiphase flow remediation processes, numerical simulation remains challenging. Previous mesoscale sandbox and sand-column experiments have explored many approaches to simulate DNAPL dissolution processes, yet only a few simulations, established based on these experimental data, have incorporated the complex mass transfer processes regulated by diverse influencing factors (Guo et al., 2020; Marble et al., 2008). Mass transfer models considering multiple factors, as well as solubilization mechanisms, have not yet been applied to existing DNAPL remediation simulations under co-solvent or surfactant flushing scenarios. Most simulations can only reproduce the behavior of a simple eluent concentration curve under the water flushing scenario (Kokkinaki et al., 2013; Zhang and Brusseau, 2004). In solubilization flushing scenarios, the mass transfer rate coefficient is often approximated as a constant to assess the average DNAPL dissolution rate (Demiray et al., 2021; Karaoglu et al., 2019). Agaoglu et al. (2012) argued that assuming a constant mass transfer coefficient for the entire flushing experiment may not be appropriate. In co-solvent or surfactant flushing scenarios, the average mass transfer rate coefficient constants fitted by numerical models are often much lower than the values calculated by mass transfer models derived from experimental observations (Aydin-Sarikurt et al., 2016; Karaoglu et al., 2019). Due to the complexity of DNAPL mass transfer, it is difficult for existing models to capture the DNAPL flushing process with complex effluent concentration behaviors, especially for enhanced DNAPL dissolution processes (Kaye et al., 2008).

At the hectometer scale, numerical simulations face significant challenges in overcoming the limitations associated with precise characterization of the contaminant source zone and high computational cost (Song et al., 2022). The upscaled analytical solution is a good alternative method. This model has the following basic assumptions when it is used to calculate contaminant fluxes at a coarser scale: (1) the unstable and non-uniform three-dimensional flow field is approximated as a stable and uniform one-dimensional flow field; (2) the model neglects the influences of the hydrodynamic dispersion and molecular diffusion on the concentration field; (3) the model does not account for the initial dissolution process of contaminants; (4) the contaminant dissolution process is considered as the pseudo steady state; (5) the upscaled mass transfer coefficient is used to describe the mass transfer behaviors of contaminants. The source zone is divided into two domains of ganglia- and pool-dominated regions to accurately predict two-stage reductions in the mass discharge as a function of mass removal (Christ et al., 2010).

In this study, we extend the multi-source zone mixed numerical model and the upscaled analytical solution model to simulate DNAPL dissolution behaviors under the following two scenarios: (1) water flushing in a complex DNAPL source configuration, and (2) co-solvent flushing with a residual DNAPL structure. The two extended models are proposed to effectively improve prediction accuracies and predict DNAPL dissolution

behaviors under solubilization conditions, which provide both theoretical insights and practical guidance for the remediation and risk management of organic contaminant sites.

1 Experiments and models

This study aimed to evaluate DNAPL dissolution processes using an improved numerical model and an improved upscaled analytical solution model, both of which were calibrated with sandbox experimental data. Two flow cell experiments were simulated: (1) a mixed-source region configuration subjected to continuous water flushing (Experiment A), and (2) a residual DNAPL source structure treated with shorter-duration pulse flushing of ethanol solution (Experiment B).

1.1 Experiment A

Difilippo et al. (2010, 2011) conducted a series of Trichloroethene (TCE) flushing experiments in flow cells to investigate the impacts of organic-liquid distribution and porous media heterogeneity on mass removal behaviors. The Mixed-Source experiment was selected as the focus of this study, in which the flow cell consisted of a homogeneous pack of 40/50 mesh sand with a 2 cm thick capillary barrier of 70/100 mesh sand along the bottom boundary. Its porosity was 0.4389. The sand media with diameters of 359 μm (40/50 mesh) and 172 μm (70/100 mesh) had representative hydraulic conductivities of 4.0 cm/min and 0.1 cm/min, respectively. The flow cell was 40 cm long, 20 cm high, and 2.6 cm wide, with multiple evenly spaced injection/extraction ports on each end. Three ports were evenly spaced at the top of the cell for injection of organic liquids. A total of 12 mL TCE was injected into the flow cell at a rate of 1 mL/min from the top central inlet and allowed to naturally distribute within the porous media for a period of 48 h to obtain a stable initial TCE distribution prior to the initiation of water flushing. Then, the de-aired water was injected at a constant rate of 3.3 mL/min.

1.2 Experiment B

Wang et al. (2019) employed a transmission light monitoring system to investigate the transport and elution behaviors of tetrachloroethylene (PCE) in a sandbox with dimensions of 20 cm× 32 cm × 1.65 cm. Multiple injection/extraction ports were evenly distributed on each end of the sandbox, resembling the flow cell from Difilippo et al. (2010, 2011). The sandbox was mainly packed with 40/50 mesh sand. The 70/80 mesh sand was packed along the bottom and top boundaries with a thickness of 1 cm. The porosity of the sandbox was 0.31. A total of 4.5 mL PCE was injected through the injection port at the top before flushing with 50% ethanol solution. Simultaneously, water was injected at a Darcy velocity of 1 m/d from the left side of the sandbox. When the PCE distribution and elution concentration reached stability after water flushing for 24 h, the pulse flushing of the ethanol solution was initiated. First, 50% ethanol solution of 3 Pore Volume (PV) was injected at a Darcy velocity of 1 m/d, followed by water flushing at the same Darcy velocity for 24 h. The above steps were repeated twice to complete the pulse flushing process. Finally, 50% ethanol solution of 9 PV was injected.

1.3 Description and improvement of the numerical model

UTCHEM (Delshad et al., 1996; Liang and Falta, 2008), a three-dimensional, multiphase, multicomponent, finite-difference numerical model was used to simulate the DNAPL remediation process in this work. Because the experiments involved complex mass transfer processes under cosolvent solubilization, some modifications including the improvement of the Hand's model (Appendix A) and the application of a new mass transfer model were made based on UTCHEM-9.0.

The DNAPL dissolution rate (R) was assumed to be represented by a linear driving force model (Powers et al., 1992):

$$R = K(C^{eq} - C_2) \tag{1}$$

Where: K is the lumped mass transfer coefficient, C^{eq} is the equilibrium concentration of DNAPL in water or microemulsion phase, and C_2 represents the effluent contaminant concentration in the aqueous phase or the microemulsion phase. Previous studies demonstrated that K depended on several factors, including the groundwater velocity, aqueous-phase composition, DNAPL saturation, and porous media properties (Hu et al., 2021; Powers et al., 1994; Wang et al., 2023a). Yang et al. (2022) obtained an empirical model for non-equilibrium mass transfer considering multiple factors based on residual PCE dissolution observations in a micropore model. The dissolution process of residual PCE was divided into three stages, namely, a strong convection stage (Stage I),

a weak convection stage (Stage II), and a diffusion stage with a limited distance (Stage III). In Stage II and Stage III, the impacts of mass transfer on elution concentrations are negligible. Thus, this study focused exclusively on Stage I. Experimental data from Yang et al. (2022) were re-fitted and the following model was obtained:

$$Sh' = \alpha S_2^{(0.8664+2.9571S_0)} Re^{1.9602} \left(1+0.01825\left(\frac{C^{eq}}{WSOL}\right)^{1.1453}\right) \quad (2)$$

Where: Re and S_2 are the Reynolds number and DNAPL saturation, respectively; S_0 represents the distribution characteristic of residual DNAPL in the system; α is a fitting parameter; $WSOL$ with a unit of volume fraction represents the solubility of DNAPL in the water phase.

Equation 2 was derived from the dissolution data of residual DNAPL, which is not suitable for characterizing the non-equilibrium mass transfer process in DNAPL pool regions. Christ et al. (2006) assumed that the mass transfer expression was a function of the average Darcy velocity and the mass reduction, and emphasized that, regardless of the model complexity, all upscaled mass transfer correlations should employ the same function form:

$$K = k_0\left(\frac{M}{M_0}\right)^{\beta} \quad (3)$$

Where: k and β are fitting parameters. M represents the DNAPL mass at time t, and M_0 denotes the initial DNAPL mass (at $t = 0$). k_0 is a function of system parameters such as the Darcy velocity and geometric dimensions of a DNAPL pool. Luciano et al. (2018) employed the geometric dimensions of a pollution source region as parameters to evaluate mass transfer processes. Stewart et al. (2022) divided a DNAPL source zone into separate mass regions and evaluated the initial geometric dimensions of each mass region as mass transfer model parameters similarly. They also assumed that the vertical dispersion was the sole mechanism in the analytical expressions for the total mass dissolution rates of DNAPL pools on a bulk scale. However, during the flushing simulation, DNAPL can migrate to other regions, increasing the geometric ranges of DNAPL pools (Fig. 1). It is inappropriate to evaluate the mass transfer process of DNAPL pools by their initial geometric dimensions, given the large-ranging migration behaviors of DNAPL pools.

In this work, the ratio $M(t)/M_0$ is equivalent to that of DNAPL saturation (S_2) to its initial saturation ($S_{2,0}$) in pool-dominated regions. The mass reduction in a DNAPL pool means that the Darcy velocity increases. To represent k_0, the mass transfer coefficient model per unit normalized interfacial area presented by Powers et al. (1994) is employed. Therefore, the mass transfer rate coefficient in a pool region is expressed as:

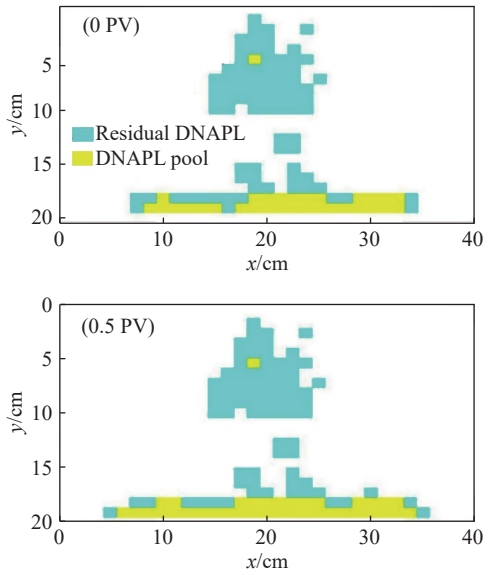


Fig. 1 Comparison of DNAPL distributions at different times (PV) in the mixed-source experiment

$$K = \begin{cases} \tau \cdot 36.8 Re^{0.654}\left(\frac{S_2}{S_{2,0}}\right)^{\beta} & (S_{2,0} \geqslant WSOL) \\ \tau \cdot 36.8 Re^{0.654}\left(\frac{S_2}{WSOL}\right)^{\beta} & (S_{2,0} < WSOL) \end{cases} \quad (4)$$

Where: τ is a fitting parameter.

1.4 Description and improvement of the upscaled analytical solution model

The contaminant flux in a complex DNAPL source zone could also be predicted using the upscaled model from Christ et al. (2010) and Song et al. (2022), which adopts a steady-state solution (Equation 5) of the one-dimensional advection-dispersion equation, coupled with an upscaled mass transfer coefficient that is a function of the initial source zone GTP (the ganglia-to-pool ratio). GTP can be re-expressed in terms of the fraction of DNAPL mass distributed in ganglia (GF) or pools (PF).

$$\overline{C}(L) = \overline{C_g}(L) + \overline{C_p}(L) \quad (5)$$

$$\overline{C_g}(L) = C^{eq}\left[1-\left(1-\frac{f_g\overline{C}_0}{C^{eq}}\right)^{\left(\frac{GF\cdot M}{GF_0\cdot M_0}\right)^{\beta_1}}\right] \quad (6)$$

$$\overline{C_p}(L) = C^{eq}\left[1-\left(1-\frac{f_p\overline{C}_0}{C^{eq}}\right)^{\left(\frac{(1-GF)\cdot M}{(1-GF_0)\cdot M_0}\right)^{\beta_2}}\right] \quad (7)$$

Where: $\overline{C}(L)$ is the average contaminant flux at a distance L down-gradient from the source zone; $\overline{C_g}(L)$ and $\overline{C_p}(L)$ represent the contaminant fluxes from the ganglia region and DNAPL pool region, respectively; $\overline{C}_0$ is the initial contaminant flux at that location; f_g and f_p represent the proportions derived from the fluxes of the DNAPL source characterized as ganglia and pools, respectively. β_1 and β_2 are fitting parameters; GF_0 denotes the initial fraction of DNAPL mass located in ganglia. The above equations are used to simulate the DNAPL flux under the scenario of water flushing.

To enhance the predictive accuracy of the upscaled model, numerical simulation results under various initial DNAPL distributions were used to revise its partial parameters, *i.e.*, GF, f_p, and f_g. Furthermore, a new upscaled mass transfer model, incorporating the DNAPL solubilization mechanism, was coupled with the upscaled analytical solution model. And the improved model of the DNAPL flux under solubilization conditions was described in Section 2.2.

1.5 Sensitivity analysis

To evaluate the influence of input parameters on the effluent concentration predicted by mathematical models, it is necessary to calculate sensitivity coefficients of distinct parameters (Karaoglu et al., 2019):

$$SC = \frac{\partial C_2}{\partial p_i}(t, p_1, p_2 \cdots p_n)\frac{p_i}{C_2} \quad (8)$$

Where: SC (sensitivity coefficients) and C_2 (effluent concentration) are functions of time (t) and all parameters (p_i). In the sensitivity analysis of the numerical model, four parameters, *i.e.*, GTP, the mass transfer rate of residual DNAPL, the mass transfer rate of DNAPL pool and the DNAPL solubility in ethanol solutions, were selected to calculate sensitivity coefficients. In the upscaled analytical solution model, GTP, β_1, β_2, f_g, γ (a power exponent fitting parameter of a ratio for the DNAPL solubility in co-solvent solution (C^{eq}) to that in water ($WSOL$), see Section 2), and the DNAPL solubility in ethanol solutions were selected to calculate sensitivity coefficients.

The sensitivity coefficient depends on the base case simulation. In this work, there were four base case simulations, namely, the numerical simulation of Experiment A, the numerical simulation of Experiment B, the upscaled simulation of Experiment A, and the upscaled simulation of Experiment B. In each sensitivity simulation, the input parameter was usually doubled from the base case value. However, for parameters with upper limits, doubling their values generally yielded abnormal simulation results, such as f_g with an upper limit of 1. Sensitivity analysis was performed using an intermediate value between the base model parameter value and its upper limit.

2 Results

2.1 Numerical model prediction

The validity of the mass transfer model considering the solubilization mechanism was evaluated by characterizing the residual DNAPL dissolution process under a complex source configuration with single water flushing (Experiment A, Difilippo et al., 2010) and under a residual source structure with pulse flushing of the ethanol solution (Experiment B, Wang et al., 2019).

The rectangular flow cell was uniformly discretized into two-dimensional grids, with 30 × 22 × 1 for Experiment A and 20 × 32 × 1 for Experiment B in the X, Z, Y directions, respectively (Fig. 2). The flow cell was assumed to be fully saturated with water. The top and bottom boundaries were set as zero flux boundaries. Vertical pseudo-wells were installed on the left and right boundaries. For the numerical simulation of Experiment A, the right boundary condition was set to an injection well with a constant flow rate ($4.752e^{-3}$ m^3/d), while the left boundary was a pumping well with a constant bottomhole pressure (101.55 kPa). The heterogeneity of the media was ignored. The elution behaviors of Experiment A were simulated under different mass transfer models, such as the multi-source zone mixing model (Equations 2 and 4), single-source zone model (Equation 2), a mass transfer rate constant (K = 15 d^{-1}), and the Imhoff model (Imhoff et al., 1995, Equation 9) (Figs. 3−4). For the numerical simulation of Experiment B, the right boundary condition was set to an extraction well with a constant bottomhole pressure (101.55 kPa), while the left boundary was an injection well with a constant flow rate ($4.752e^{-3}$ m^3/d). Various mass transfer models, such as the single-source zone model (Equation 2), the Imhoff model, and the constant mass transfer rate coefficient (K = 6.5 d^{-1}), were utilized to estimate the dissolution process of PCE (Figs. 3−4). The details of the model parameters are listed in Table 1 and Table 2.

$$Sh' = \tau Re^{0.75}\left(\frac{S_n}{\varphi}\right)^{\beta} Sc^{0.5} \quad (9)$$

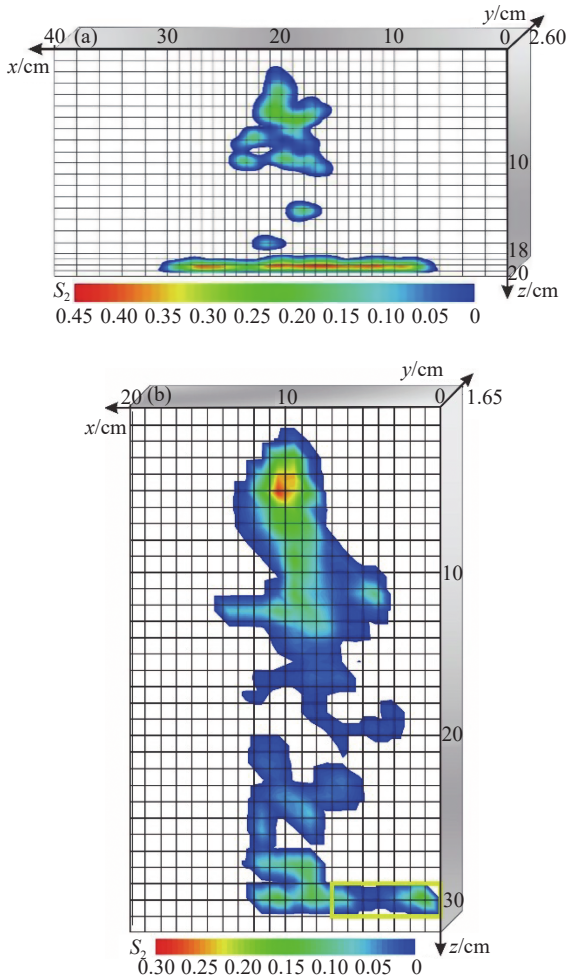


Fig. 2 The initial DNAPL distribution before flushing

Notes: a-mesh generation for Experiment A; b-mesh generation for Experiment B

It should be noted that during the first flushing of ethanol solution and water in Experiment B, there was slight migration of PCE in the region marked by the yellow curve in Fig. 2. Despite the relatively low DNAPL saturation within the marked zone (maximum saturation of 0.15), DNAPL migration behavior was observed in the simulation. This may be attributed to the model's inadequate consideration of the heterogeneity of media. The DNAPL migration proportion (MP, the ratio of DNAPL migration volume to the DNAPL volume in the yellow curve in Fig. 2) exhibited a high value in the early stage of the simulation, followed by rapid decline and subsequent fluctuation (Fig. 5). Although the average contribution ratio of DNAPL in the marked region to effluent concentrations was 18.5%, the average DNAPL migration proportion in that zone was only 2.6 ‰. Therefore, DNAPL migration in this region can be ignored in predictions of the effluent concentration and PCE mass removal.

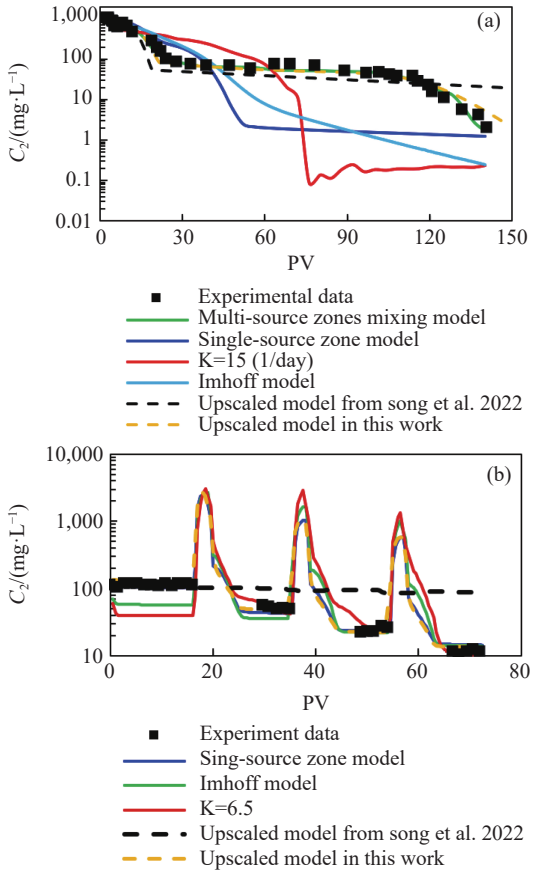


Fig. 3 The simulated elution concentration (C_2) from the upscaled analytical solution model and numerical model, respectively

Notes: a-Experiment A; b-Experiment B

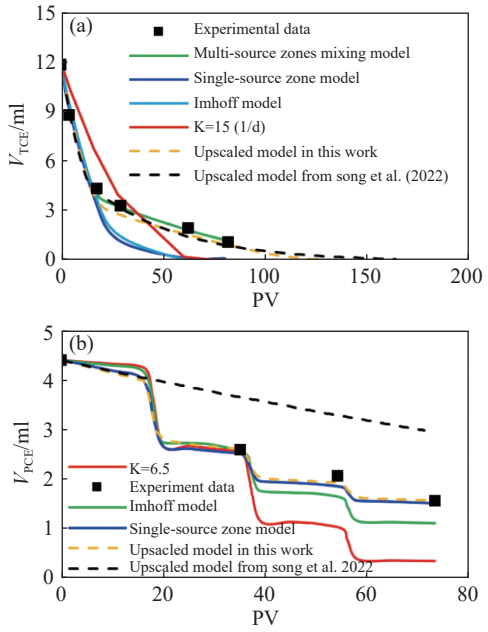


Fig. 4 The remaining DNAPL volume (V) in the flow cell varying with the pore volume of injected flushing fluid (PV)

Notes: a-Experiment A; b-Experiment B

Table 1 List of key parameters used in numerical simulations

Parameter	Classification	Value	
		Mixed-source experiment (Experiment A)	Pulse flushing experiment (Experiment B)
Permeability/(cm/min)	70/100 (or 70/80) mesh	0.10[a]	0.13[d]
	40/50 mesh	4.00[a]	12.21[h]/4.00[b]
Residual saturation	Low capillary number		
	DNAPL phase (S_{r2})	0.20[a]	0.12[b]
	Aqueous phase (S_{r1})	0.10[c]	0.10[c]
	Microemulsion phase (S_{r3})	-	0.10[c]
	High capillary number		
	DNAPL phase (S_{r2})	0.00	0.00
	Aqueous phase (S_{r1})	0.00	0.00
	Microemulsion phase (S_{r3})	-	0.00
Endpoint relative permeability	Low capillary number		
	DNAPL phase (k^o_{r2})	0.37[c]	0.37[c]
	Aqueous phase (k^o_{r1})	1.00[c]	1.00[c]
	Microemulsion phase (k^o_{r3})	-	1.00[c]
	High capillary number[j]		
	DNAPL phase (k^o_{r2})	1.00	1.00
	Aqueous phase (k^o_{r1})	1.00	1.00
	Microemulsion phase (k^o_{r3})	-	1.00
Relative permeability exponent	Low capillary number		
	DNAPL phase	5.00[h]	5.00/3.50[h]
	Aqueous phase	2.85[e]	2.85[e]
	Microemulsion phase	-	2.85[e]
	High capillary number[j]		
	DNAPL phase	1.00	1.00
	Aqueous phase	1.00	1.00
	Microemulsion phase	-	1.00
Capillary pressure endpoint/kPa		2.90[d]	2.90[d]
Capillary pressure exponent		–0.50[d]	–0.50[d]
Density/(g/mL)	DNAPL (TCE/PCE)	1.460[f]	1.622[f]
	Water	0.998[f]	0.998[f]
	Ethanol	-	0.787[f]
Interfacial tension of water-oil/(dyn/cm)		35.62[g]	45.00[i]
Interfacial tension between ethanol solution and PCE phase/(dyn/cm)	$\sigma = \sigma_0 e^{-4.1611 C_{31}}$[k]		
viscosity of ethanol + water + PCE mixture/(Pa·s)	$\mu_l = C_{1l}\mu_{1,0}e^{1.8132(C_{2l}+C_{3l})} + C_{2l}\mu_{2,0}e^{0.9646(C_{1l}+C_{3l})} + C_{3l}\mu_{3,0}e^{(1.5823C_{1l}-1.5125C_{2l})}$[l]		
Longitudinal dispersion/m		0.015[g]	0.015[g]
Transverse dispersion/m		0.008[g]	0.008[g]

[a] DiFilippo et al., (2010); [b] Schroth et al., (1996); [c] Grant, (2005); [d] Guo et al., (2018); [e] Liao et al., (2016); [f] NIST Chemistry WebBook; [g] Aydin-Sarikurt et al., (2016); [h] Correction parameters for medium permeability and relative permeability within PCE migration zone (i.e., the region marked by yellow curve in Fig. 2) in pulse flushing experiment; [i] Demiray et al., (2021); [j] Agaoglu et al., (2012); [k] Interfacial tension is a function of ethanol content. the experimental data come from Hayden et al., (1999) and Lunn and Kueper, (1997); [l] The viscosity of ethanol + water + PCE mixture is calculated in terms of the viscosity of the pure phases. The viscosity data of PCE-C_2H_5OH, H_2O-C_2H_5OH, and H_2O-C_2H_5OH-PCE systems come from Agarwal and Singh, (2004), Khattab et al., (2012), and Hayden et al., (1999), respectively.

Table 2 Calibrated parameters for different mass transfer models

Experiment	Mass transfer model	Parameter				
		α	S_0	K (1/d)	τ	β
Mixed-Source experiment	Multi-Source zones mixing model (Equations 2 and 4)	70,000	0.00	-	6.51	0.10
	Single-Source zone model (Equation 2)	70,000	0.00	-	-	
	Imhoff model (Equation 9)	-			1.50	1.00
	K	-		15.00	-	
Pulse flushing	Single-Source zone model (Equation 2)	630,000	0.49	-	-	
	Imhoff model (Equation 9)	-	-	-	2.00	1.19
	K	-		6.50	-	

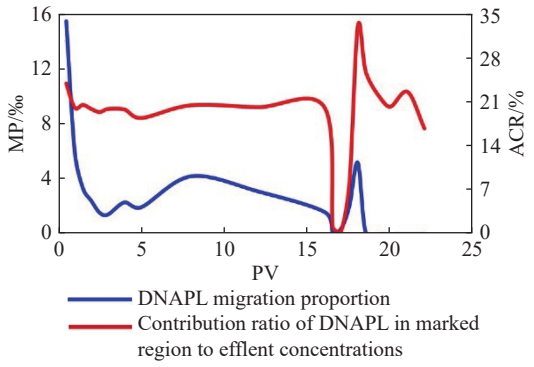


Fig. 5 DNAPL Nigration Proportion (MP) and average contribution ratio of DNAPL to effluent concentrations in the marked zone (ACR)

2.2 Upscaled model prediction

There are six parameters for contaminant flux calculations in the upscaled model (Equation 5): $\overline{C}_0$, f_g, f_p, β_1, β_2, and GF. Christ et al. (2010) and Song et al. (2022) represented β_1 as a function of GTP ($\beta_1 = 1.07\mathrm{GTP}^{-0.25}$). The mass depletion from pool-dominated regions was assumed essentially constant until near complete mass removal (β_2 = 0.50). The evolution of the Ganglia Fraction (GF) was a function of mass removal (Equation 10):

$$GF = \begin{cases} GF_0\left[1-\left(\dfrac{1-\dfrac{M}{M_0}}{GF_0}\right)^{7.8}\right] & \left(1-\dfrac{M}{M_0}\right) \leqslant GF_0 \\ 0 & \left(1-\dfrac{M}{M_0}\right) > GF_0 \end{cases} \tag{10}$$

The area ratio of DNAPL pool projected onto the lower gradient control plane was used to characterize the initial fraction of the contaminant flux eluting from DNAPL pool regions (f_p), and $f_g + f_p = 1$.

2.2.1 Prediction of Experiment A

The simulated elution curve under the mixed-source configuration by the upscaled analytical solution model from Song et al. (2022) was shown in Fig. 3. Although the model could predict multi-stage behaviors of DNAPL dissolution under complex source configurations, its predictive performance remained limited. Particularly in the stage subsequent to complete dissolution of the initial DNAPL ganglia zone ($\left(1-\dfrac{M}{M_0}\right) > GF_0$), the predicted result showed a linear decrease in DNAPL elution concentration. Moreover, the upscaled analytical solution model predicted that the second stage of the elution curve would be initiated earlier.

In fact, when $\left(1-\dfrac{M}{M_0}\right) > GF_0$, there remains a certain proportion of undissolved DNAPL ganglia in the contaminated source zone. In this work, the numerical model (multi-source zone mixing model), calibrated with experimental data, was used to calculate the elution behaviors under different initial DNAPL distributions (GTP, Fig. 6). When the elution curve entered the second stage, the removal ratio of DNAPL ($1-M/M_0$) in the contaminated region was significantly higher than the initial proportion of DNAPL ganglia (GF_0). The difference (ω) between $1-M/M_0$ and GF_0 is linearly correlated with GF_0 (Fig. 7). Thus, in this work, the evolution function of the Ganglia Fraction (GF) was represented as:

$$GF = \begin{cases} (GF_0+\omega)\left[1-\left(\dfrac{1-\dfrac{M}{M_0}}{GF_0+\omega}\right)^{7.8}\right] & \left(1-\dfrac{M}{M_0}\right) \leqslant (GF_0+\omega) \\ 0 & \left(1-\dfrac{M}{M_0}\right) > (GF_0+\omega) \end{cases} \tag{11}$$

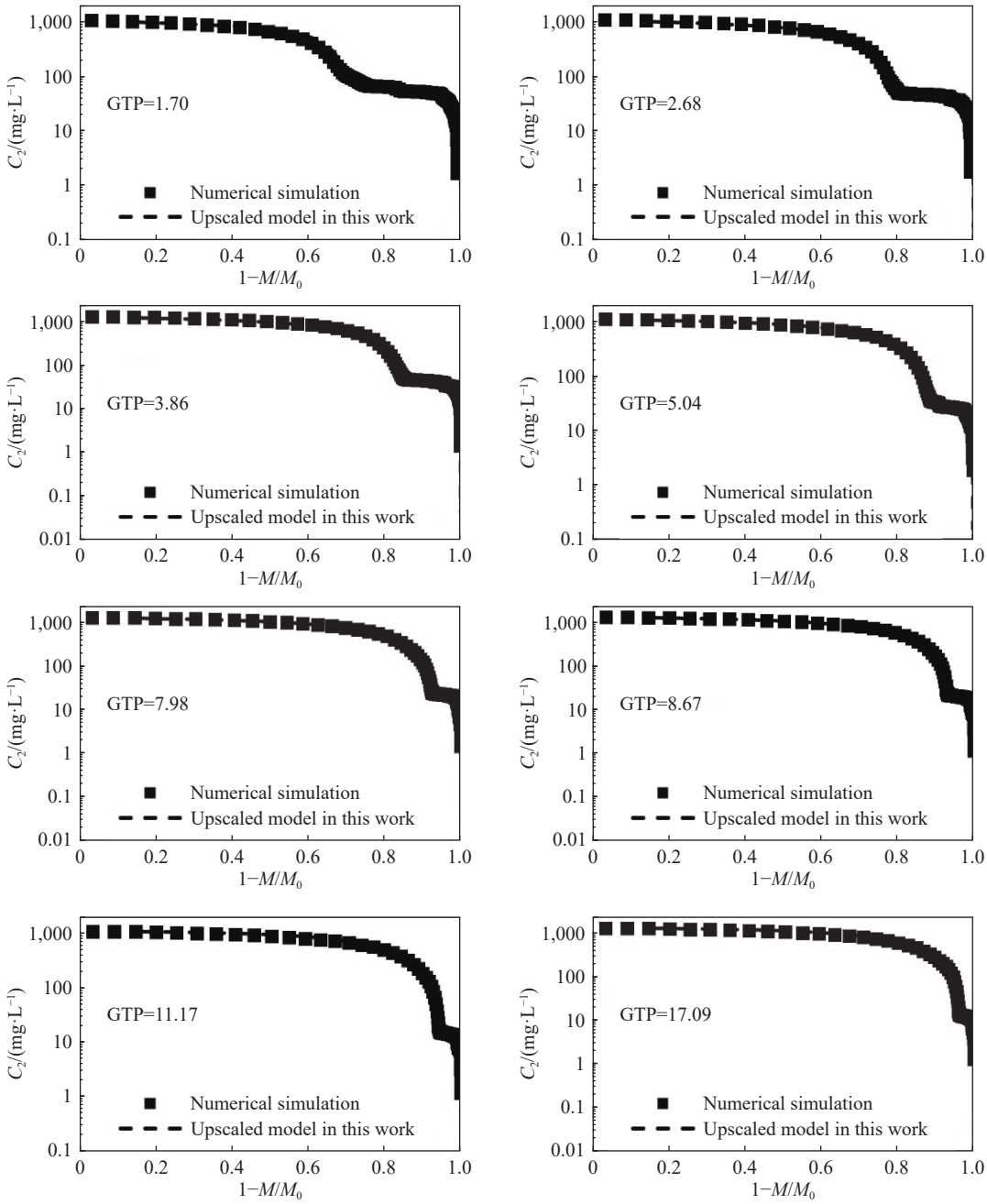


Fig. 6 Under different initial DNAPL distributions (GTP), the prediction of elution concentration (C_2), from the upscaled analytical solution model and the numerical model (multi-source zone mixing model), varying with DNAPL depletion ratio ($1-M/M_0$)

$$\omega = -0.3045GF_0 + 0.3059 \tag{12}$$

Where: ω is a correction coefficient, representing the difference between the mass depletion of DNAPL, when the DNAPL ganglia in source regions are completely dissolved, and GF_0. It was assumed that the contribution ratio (f_p) of the DNAPL pool to the elution concentration remained constant in the studies of Christ et al. (2010) and Song et al. (2022). After the dissolution dominated by DNAPL pool became the sole contributor to effluent concentration, the decay pattern of effluent concentration (Equation 7) was different from that of DNAPL ganglia dominated stage (Equation 6). Additional parameter calibration (η) for f_p was required. Using the upscaled analytical solution model to fit the elution curves predicted by the numerical model under different GTPs, the proportion of the flux from the DNAPL pools (f_p) is expressed as:

$$f_p = (1 - f_g) \cdot \eta \tag{13}$$

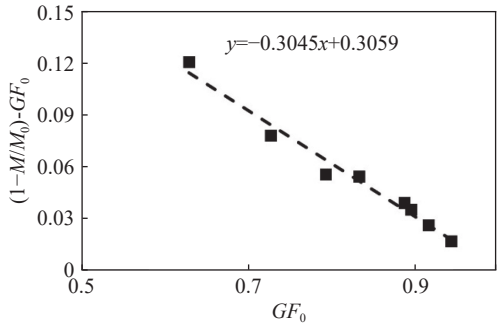


Fig. 7 The relationship between the removal ratio of DNAPL in the contaminated region, *i.e.,* $(1-M/M_0)$, and the initial proportion of DNAPL ganglia (GF_0) when the elution curve enters the second stage

$$\eta = 1 + (-21.348GF_0^2 + 42.334GF_0 - 14.589)\left(1-\frac{M}{M_0}\right)^{\left(740.83GF_0^2-990.59GF_0+345.31\right)} \quad (14)$$

Under different initial DNAPL distributions (Fig. 6, GTP), the fitting parameter (f_g) of the upscaled model (Equations 5, 11, and 13) was a function of GTP (Fig. 8). It was lower than the area ratio of DNAPL ganglia projected onto the lower gradient control plane (f_g =0.900 from Song et al., 2022; Fig. 8). By adjusting β_2, the new upscaled model (Equations 5, 11, and 13) could effectively capture the multi-stage dissolution behaviors of DNAPL under complex source structures (Figs. 3−4). The detailed parameters were listed in Appendix A Table S2. The contribution ratios of DNAPL ganglia and pool to the elution flux were derived from corresponding dissolution rates, respectively (Equations 6 and 7).

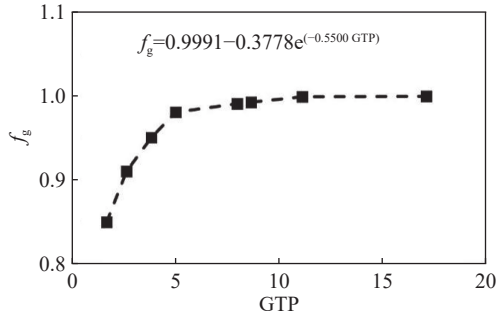


Fig. 8 The relationship between the proportion of the flux from DNAPL ganglia (f_g) and the initial DNAPL distribution (GTP)

2.2.2 Prediction of Experiment B

As shown in Figs. 3 and 4, the upscaled analytical solution model from Song et al. (2022) was unable to simulate the elution curve behaviors during ethanol solution flushing. This could be explained by the derivation process of the upscaled model (Equation 5, Song et al., 2022; Christ et al., 2010). The upscaled mass transfer coefficient (κ_{eff}) was a simple power function of the relative groundwater velocity and relative DNAPL mass (Equation 15), without considering the influence of DNAPL solubilization on the mass transfer process.

$$\kappa_{eff} = \kappa_0\left(\frac{\overline{q}}{\overline{K}}\right)\left(\frac{M(t)}{M_0}\right)^{\beta} \quad (15)$$

Where: $\overline{q}$ is the average one-dimensional hydraulic flux; $\overline{K}$ is the average hydraulic conductivity; κ_0 is the fitting parameter.

According to the new mass transfer empirical formula (Equation 2), the upscaled mass transfer coefficient could also be expressed as a function of the relative solubility of DNAPL (the solubility ratio of DNAPL in co-solvent solutions (C^{eq}) to that in water ($WSOL$)). In this work, it is simplified as:

$$\kappa_{eff} = \kappa_0\left(\frac{\overline{q}}{\overline{K}}\right)\left(\frac{M(t)}{M_0}\right)^{\beta}\left(\frac{C^{eq}}{WSOL}\right)^{\gamma} \quad (16)$$

Where: γ is a fitting parameter. When the contaminated region is flushed by water, the upscaled mass transfer coefficient (Equation 16, $\frac{C^{eq}}{WSOL}=1$) reduces into Equation 15. Then, following the derivation approach of Song et al. (2022) and Christ et al. (2010), the flux ($\overline{C}(L)$) at the downstream boundary ($x = L$) of the contaminated source zone is obtained by:

$$\overline{C}(L) = C^{eq}\left[1-\left(1-\frac{\overline{C}_0}{C^{eq}}\right)^{\left(\frac{M}{M_0}\right)^{\beta}\left(\frac{C^{eq}}{WSOL}\right)^{\gamma}}\right] \quad (17)$$

Similarly, by partitioning the contaminated source zone into ganglia- and pool-dominated regions, $\overline{C}(L)$ can be expressed as the sum of the weighted fluxes from the ganglia-dominated DNAPL region and the one from pool-dominated DNAPL region:

$$\overline{C}(L) = C^{eq}\left[2-\left(1-\frac{f_g\overline{C}_0}{C^{eq}}\right)^{\left(\frac{GF\cdot M}{GF_0\cdot M_0}\right)^{\beta_1}\left(\frac{C^{eq}}{WSOL}\right)^{\gamma}} - \left(1-\frac{f_p\overline{C}_0}{C^{eq}}\right)^{\left(\frac{(1-GF)\cdot M}{(1-GF_0)\cdot M_0}\right)^{\beta_2}\left(\frac{C^{eq}}{WSOL}\right)^{\gamma}}\right] \quad (18)$$

The GTP in Experiment B was 2.4. Hence, f_g was 0.898, according to the relationship between f_g and GTP (Fig. 8). It was evident that the new upscaled analytical solution model could accurately predict the DNAPL elution behaviors under

the pulse flushing of ethanol solution when upscaled mass transfer model could characterize variations in DNAPL solubilization capacity (Fig. 3 and 4).

3 Discussion

3.1 The improvement for the two models

In numerical simulations, mass transfer processes for ganglia- and pool-dominated DNAPL source zones were evaluated, respectively. Furthermore, the impact of variations in DNAPL solubility on the mass transfer process was incorporated into the mass transfer model. It was a well-established consensus that the non-singular dissolution behavior of DNAPL was caused by the complex source zone structure (Guo et al., 2020; Stewart et al., 2022). In addition, abrupt changes in the DNAPL solubility under the pulse flushing of cosolvents or surfactants could also result in the complex dissolution behaviors. Apart from the improved mass transfer model in this work, other models were unable to adequately characterize the mass transfer behaviors of distinct DNAPL source regions and also failed to describe such behaviors under the condition of abrupt changes in DNAPL solubility. In the simulation of Experiment A, other mass transfer models overestimated the dissolution rate of the DNAPL pool-dominated zone. In the simulation of Experiment B, they failed to accurately evaluate the DNAPL dissolution rates during both the ethanol solution flushing stage and water flushing stage.

The upscaled model in this study was an improvement based on the model from Song et al. (2022). In the simulations of Experiments A and B, the prediction accuracies of the new upscaled model were improved by approximately 48% and 84%, respectively. In the research on the upscaled model presented in this paper, it was proposed that a certain proportion of residual DNAPL still remained in the contamination source zone when the DNAPL mass removal ratio ($1-\frac{M}{M_0}$) exceeded the initial DNAPL ganglion mass fraction (GF_0). Therefore, the calculation of the ganglia fraction of the upscaled model from Song et al. (2022) has been revised. Additionally, this work argued that it was inappropriate to approximate the contribution ratio (f_g) of DNAPL ganglia to the contaminant flux using the area ratio of the initial DNAPL ganglia projected onto the lower gradient control plane. Furthermore, if the upscaled model failed to account for the impact of DNAPL solubility on mass transfer behaviors, it could not accurately reproduce the effluent concentration dynamics during ethanol pulse flushing and thus could not provide reliable guidance for the enhanced remediation of DNAPL-contaminated sites.

3.2 Sensitivity analysis

To gain insights into the impact of the key input parameters, sensitivity coefficients were calculated. The sensitivity simulation results of input parameters are presented in Fig. 9. In different base case simulations, the sensitivity coefficient of the same parameter may show diverse behaviors due to the significant differences in elution curve behaviors. For example, the sensitivity coefficients of GTP showed different time-dependent characteristics in the upscaled simulations of Experiment A and B (Figs. 9c and 9d). Furthermore, the overlapping influences of residual DNAPL and DNAPL pool on the effluent concentration also changed due to variation in the input parameter.

In numerical simulations, sensitivity coefficients of four parameters, i.e., GTP, the mass transfer rate in residual DNAPL regions, the one in DNAPL pool regions, and DNAPL solubility in ethanol solutions, exhibited varying amplitude fluctuations at critical transition regions, specifically, the shift from ganglia-dominated to pool-dominated DNAPL dissolution, as well as the switch from water flushing to ethanol solution pulse flushing (Figs. 9a and 9b). Changes in input parameters resulted in divergent dissolution rates across different DNAPL source zones, thereby causing asynchrony between the simulated plume effluent concentrations and the base model results. In addition, the fluctuation amplitudes of sensitivities for different parameters varied at critical transition regions. In contrast, they remained relatively stable during other periods. During the dissolution stage dominated by the DNAPL pool, the sensitivity coefficient of the mass transfer rate in DNAPL pool region exhibited stable positive sensitivity within 30–70 PV and stable negative sensitivity within 90–140 PV. In fact, except for fluctuations at critical transition regions, the sensitivity coefficient of the mass transfer rate in DNAPL pool region remained relatively stable in other stages. Only at 90 PV, the DNAPL pool was completely dissolved, resulting in a conversion of the sensitivity coefficient to the relatively stable

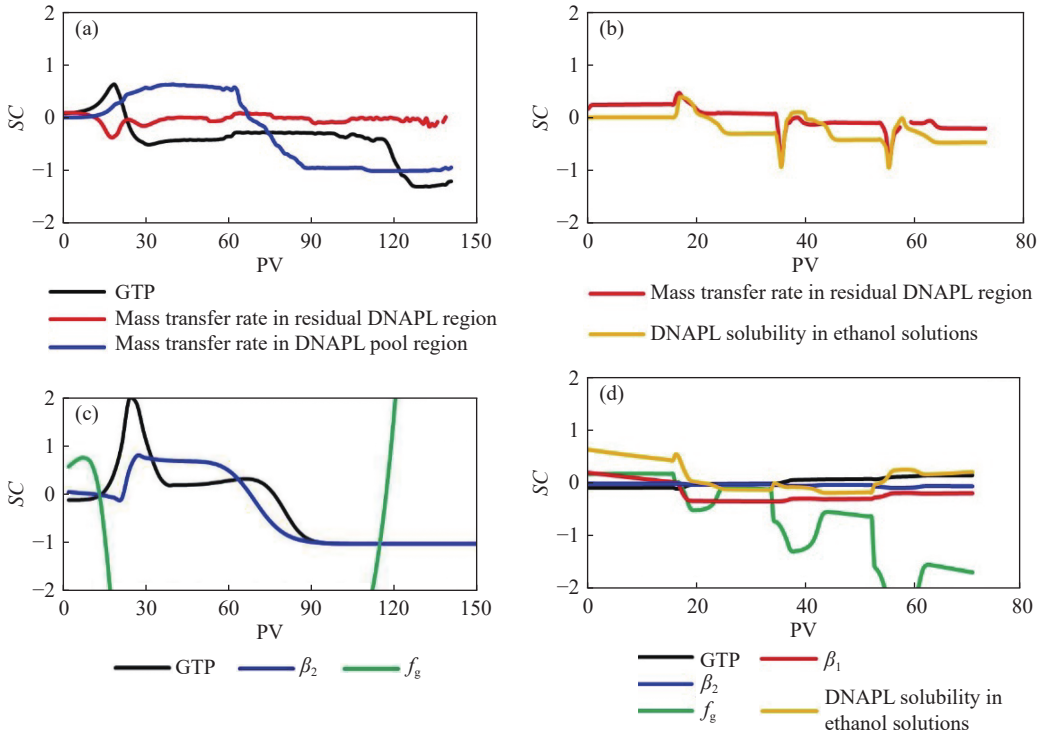


Fig. 9 Sensitivity Coefficients (*SC*) of key parameters for the numerical model predicting the effluent concentration under

Notes: (a) the mixed-source configuration and (b) the pulse flushing of ethanol solutions, for the upscaled analytical solution model predicting the effluent concentration under (c) the mixed-source configuration and (d) the pulse flushing of ethanol solutions

and negative value.

The sensitivity coefficient behaviors of input parameters in upscaled simulation were similar to that in numerical simulations at critical transition regions (Fig.9c and 9d). However, at critical transition regions, the fluctuation patterns of sensitivity coefficients of some input parameters in upscaled simulations, were more chaotic than that in numerical simulations. The above phenomena could be explained by the structural differences between the numerical model and upscaled model. In numerical simulations, the mass transfer parameters in the residual DNAPL region and the DNAPL pool region were independent and did not affect each other's DNAPL mass fluxes. However, in upscaled simulations, the DNAPL mass fluxes of the both source regions were functions of M/M_0. Variations in mass transfer parameters in each source region would mutually affect the mass fluxes of the respective source regions.

In the numerical simulation, effluent concentrations for Experiment A were most sensitive to the mass transfer rate in DNAPL pool region, followed by GTP. For Experiment B, the highest sensitivity was the DNAPL solubility in ethanol solutions. In the upscaled simulation, for Experiment A, f_g had the greatest impact on predicting effluent concentrations, followed by GTP and β_2. In the upscaled simulation of Experiment B, f_g also had the greatest impact.

3.3 Comparison between the two improved models

3.3.1 Comparison in model prediction accuracy

The numerical model exhibited superior predictive performance compared to the upscaled model. In the simulation of Experiment A, the numerical model predicted the effluent concentration variation at a time interval of 4.00 Pore Volumes (PV), with a Root Mean Square Error (RMSE) of 36.95 mg/L and a Mean Absolute Error (MAE) of 20.68 mg/L, respectively. The upscaled model predicted the effluent concentration variation at a time interval of 2.72 PV, yielding an RMSE of 85.75 mg/L and an MAE of 33.29 mg/L, respectively. In the simulation of Experiment B, the numerical model and upscaled model predicted the effluent concentration during the water flushing stage at a time interval of 0.50 PV. Consistent with Experiment A, the numerical model exhibited relatively lower prediction errors (Table 3).

The numerical model was derived from rigor-

Table 3 Root Mean Square Errors (RMSE) and Mean Absolute Errors (MAE) of effluent concentration predictions by different models

	Numerical model		Upscaled analytical solution model	
	Experiment A	**Experiment B**	**Experiment A**	**Experiment B**
RMSE/(mg/L)	36.95	7.92	85.75	10.01
MAE/(mg/L)	20.68	6.93	33.29	8.60

ous mathematical and physical equations, requiring a large number of input parameters (Tables 1 and 2). In this study, the medium was assumed to be homogeneous, which may have introduced some prediction errors. The upscaled model not only failed to account for the medium heterogeneity, but also simplified the three-dimensional (3D) mathematical and physical equations into a steady-state solution (Equation 5) of the one-dimensional advection-dispersion equation, resulting in relatively high prediction errors. In practical applications, the upscaled model offers broader utility. It requires fewer parameters and can effectively predict changes in subsurface contaminant fluxes. Thus, reliable data can be provided for designers of contaminated site remediation projects. Due to the complex structure and the large amount of input data required for the numerical model, it has greater limitations in practical field applications, such as high computational cost and the need for precise characterizations of contaminant sources. Nonetheless, the numerical model plays an irreplaceable role in theoretical research.

3.3.2 Comparison in combined contaminant fluxes from different sources

The contaminant source zone configuration dominated by DNAPL ganglia governs the elution behavior of the first stage with high contaminant fluxes, whereas that dominated by DNAPL pools determines the elution behavior of the second stage with low contaminant fluxes. The higher the GTP, the later the initiation time and lower contaminant flux of the second stage dissolution process (Fig. 6). It was well established that, for DNAPL remediation simulation with mixed source configuration (Experiment A), the average eluent concentration was the combined contaminant flux from pool- and ganglia-source regions (Fig. 10). In the initial stage, the DNAPL ganglia-dominated source zone contributed a large proportion of the contaminant flux. As flushing proceeded, the number of DNAPL ganglia decreased rapidly, and the contribution ratio to the contaminant flux gradually declined. When the contaminant flux from DNAPL ganglia decreased to the same order of magnitude as that from DNAPL pools, the combined contaminant flux declined gradually and steadily. The contaminant flux from DNAPL pools fluctuated within the range of 10–30 mg/L for a long time, due to the low dissolution rate of DNAPL pools. Numerical model prediction showed that the dissolution of the ganglia-dominated contaminant source zone persisted throughout the flushing process. Moreover, the contribution of the contaminant flux from the ganglia-dominated source zone to the combined flux in the second stage of the elution curve could not be ignored. This contribution was approximately evaluated by the mass ratio of DNAPL dissolved in different contaminant source regions. However, in the prediction from

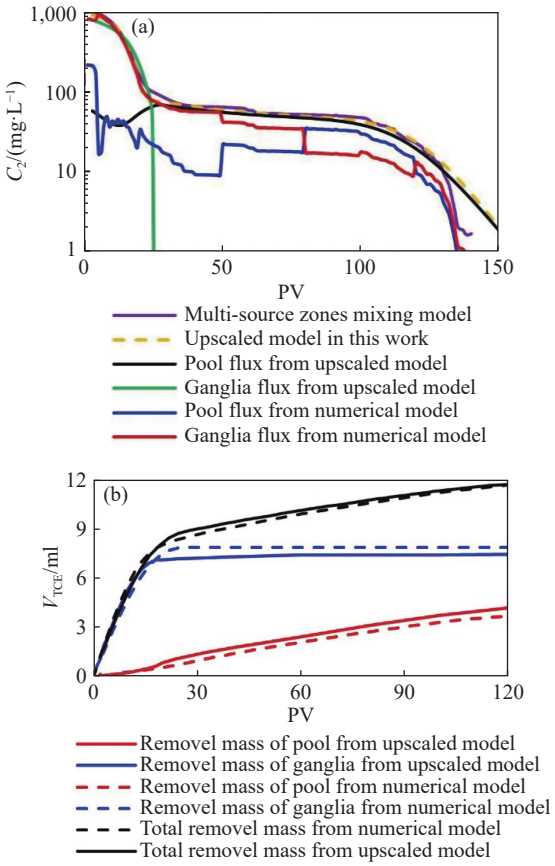


Fig. 10 Contaminant fluxes (C_2, a) and removal mass (V_{TCE}, b) from the pool- and ganglia-dominated DNAPL source regions predicted by the upscaled analytical solution model and the numerical model in Experiment A

the upscaled analytical solution model, that contribution occurred only in the first stage of the elution curve.

For the flushing process of ethanol solution, the contaminant concentration of the eluent was also the sum of the contaminant concentrations from pool- and ganglia-source regions (Fig. 11). However, in numerical simulations, it was assumed that the entire pollution source region was dominated by ganglia. Due to the high GTP of the initial DNAPL distribution (GTP=2.4) and the short flushing time (< 80 PV), in upscaled simulations, the ganglia-dominated contaminant source region was not completely dissolved before the flushing was completed. There were four stages for water flushing and 3 stages for ethanol solution flushing in total, respectively. In the first two ethanol solution flushing stages, the primary contaminant concentration of the eluent originated from the dissolution of the ganglia-dominated source region. When the ethanol solution flushing proceeded to the third stage, the contribution of the dissolution of the pool-dominated source region was not negligible. However, the contribution of the dissolution from the ganglia-dominated source region to the contaminant concentration gradually decreased when water flushing proceeded to the third and fourth stages.

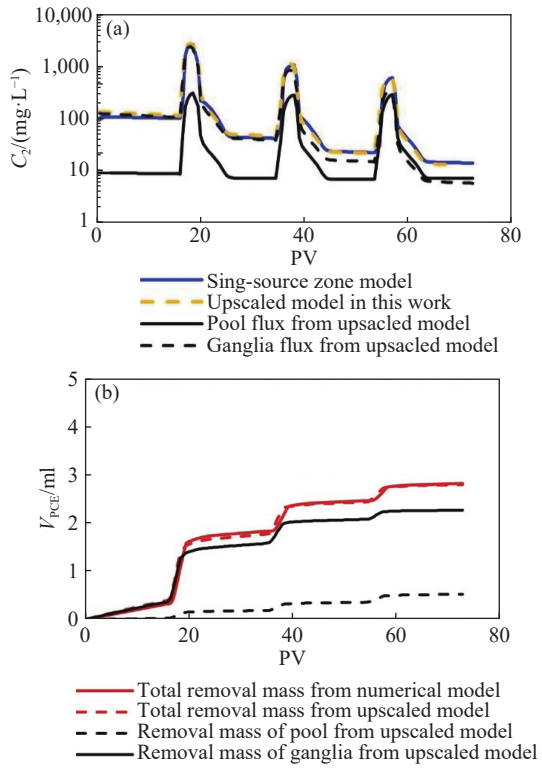


Fig. 11 Contaminant fluxes (C_2, a) and removal mass (V_{PCE}, b) from the pool- and ganglia-dominated DNAPL source regions predicted by the upscaled analytical solution model and the numerical model in Experiment B

The improved numerical model and upscaled model proposed in this study could predict the dissolution process of DNAPL under solubilization conditions. As shown in Fig. 3, when neither model accounted for variations in DNAPL solubility, the simulations failed to accurately predict the PCE concentration behaviors during water flushing following each ethanol pulse flushing. Notably, the upscaled model without considering variations in DNAPL solubility could not capture the sharp increase in DNAPL concentration in the effluent during ethanol pulse flushing. Aydin-Sarikurt et al. (2016) emphasized that published correlations did not accurately estimate the interphase mass transfer rate in the presence of cosolvents. These correlations did not incorporate fluid properties such as the density, viscosity, and diffusion coefficient. DNAPL solubility, also a fluid property, affected the mass transfer behavior of DNAPL.

4 Conclusion

In complex large-scale multiphase flow dissolution system, combining the macroscopic DNAPL source-zone configuration with DNAPL mass transfer formulations that consider multiple influencing factors is essential for accurately describing the DNAPL dissolution processes. In this work, it was demonstrated that both the improved multi-source region numerical model and upscaled analytical solution model could successfully simulate the multi-stage DNAPL dissolution behaviors under complex source region configurations and solubilization conditions. The simulation results showed that the accuracy of numerical predictions was significantly higher than that of upscaled simulations. Thus, the numerical model plays a vital role in theoretical studies, with the capability to accurately characterize contaminant sources and mass transfer mechanisms. In practical applications, upscaled simulations have wider potential in contaminated site remediation projects, due to their simple model structure, fewer input parameters, and lower computational cost. Overall, this study provides theoretical insights for developing a more robust modeling approach for the DNAPL dissolution process in large and complex systems.

Acknowledgements

This research was supported by the Qinghai Insti-

tute of Technology "Kunlun Talents" Talent Introduction Research Project (2023-QLGKLYCZX-002), the Qinghai Institute of Technology New Teacher Thesis Extension Research and Cultivation Project (2023011wys005), the National Natural Science Foundation of China (42177077).

References

Agaoglu B, Scheytt T, Copty NK. 2012. Laboratory - scale experiments and numerical modeling of cosolvent flushing of multicomponent NAPLs in saturated porous media. Journal of Contaminant Hydrology, 140: 80−94. DOI：10.1016/j.jconhyd.2012.07.005.

Agarwal D, Singh M. 2004. Densities and viscosities of binary liquid mixtures of trichloroethylene and tetrachloroethylene with some polar and nonpolar solvents. Journal of Chemical and Engineering Data, 49(5): 1218−1224. DOI：10.1021/je034203p.

Aydin-Sarikurt D, Dokou Z, Copty NK, et al. 2016. Experimental investigation and numerical modeling of enhanced DNAPL solubilization in saturated porous media. Water, Air and Soil Pollution, 227(12): 441. DOI：10.1007/s11270-016-3136-0.

Cho J, Annable MD, Rao PSC. 2005. Measured mass transfer coefficients in porous media using specific interfacial area. Environmental Science and Technology, 39(20): 7883−7888. DOI：10.1021/es0505043.

Christ JA, Ramsburg CA, Pennell KD, et al. 2006. Estimating mass discharge from dense nonaqueous phase liquid source zones using upscaled mass transfer coefficients: An evaluation using multiphase numerical simulations. Water Resources Research, 42(11): 2006WR004886. DOI：10.1029/2006WR004886.

Christ JA, Ramsburg CA, Pennell KD, et al. 2010. Predicting DNAPL mass discharge from pool-dominated source zones. Journal of Contaminant Hydrology, 114(1-4): 18−34. DOI：10.1016/j.jconhyd.2010.02.005.

Corapcioglu MY, Yoon S, Chowdhury S. 2009. Pore-scale analysis of NAPL blob dissolution and mobilization in porous media. Transport in Porous Media, 79(3): 419−442. DOI：10.1007/s11242-008-9331-8.

Delshad M, Pope GA, Sepehrnoori K. 1996. A compositional simulator for modeling surfactant enhanced aquifer remediation, formulation. Journal of Contaminant Hydrology, 23(4): 303−327. DOI：10.1016/0169-7722(95)00106-9.

Demiray Z, Akyol NH, Copty NK. 2021. Experimental assessment and modeling of enhanced solubilization of pool-dominated tetrachloroethene source zone in heterogeneous porous media. Water Air and Soil Pollution, 232(12): 516. DOI：10.1007/s11270-021-05454-z.

DiFilippo EL, Carroll KC, Brusseau ML. 2010. Impact of organic-liquid distribution and flow-field heterogeneity on reductions in mass flux. Journal of Contaminant Hydrology, 115(1-4): 14−25. DOI：10.1016/j.jconhyd.2010.03.002.

DiFilippo EL, Brusseau ML. 2011. Application of light reflection visualization for measuring organic-liquid saturation for two-phase systems in two-dimensional flow cells. Environmental Engineering Science, 28(11): 803−809. DOI：10.1089/ees.2010.0471.

Feng SJ, Niu JG, Shi FJ, et al. 2025. Remediation effectiveness and mechanism on surfactant-enhanced remediation of low-permeability petroleum hydrocarbon contaminated soil under fracturing conditions. Journal of Hydrology, 650: 132539. DOI：10.1016/j.jhydrol.2024.132539.

Grant GP. 2005. The evolution of complex DNAPL releases: Rates of migration and dissolution. Ph. D. thesis. Scotland: University of Edinburgh.

Grant GP, Gerhard JI. 2007. Simulating the dissolution of a complex dense nonaqueous phase liquid source zone: Model to predict interfacial area. Water Resources Research, 43(12): 130−139. DOI：10.1029/2007WR006038.

Guo QZ, Zhang Y, Jiang BL, et al. 2018. Experiment and numerical simulation of surfactant-enhanced aquifer remediation in PCE contaminated laboratory sandbox. China Environmental Science, 38(9): 3398−3405. (in Chinese) DOI：10.19674/j.cnki.issn1000-6923.2018.0367.

Guo ZL, Russo AE, DiFilippo EL, et al. 2020. Mathematical modeling of organic liquid

dissolution in heterogeneous source zones. Journal of Contaminant Hydrology, 235: 103716. DOI：10.1016/j.jconhyd.2020.103716.

Hayden NJ, Diebold J, Noyes G. 1999. Phase behavior of chlorinated solvent water alcohol mixtures with application to alcohol flushing. Journal of Chemical and Engineering Data, 44(5): 1085−1090. DOI：10.1021/je980273y.

Hu YX, Patmonoaji A, Xu HP, et al. 2021. Pore-scale investigation on nonaqueous phase liquid dissolution and mass transfer in 2D and 3D porous media. International Journal of Heat and Mass Transfer, 169: 120901. DOI：10.1016/j.ijheatmasstransfer.2021.120901.

Huo LL, Liu GS, Yang X, et al. 2020. Surfactant-enhanced aquifer remediation: Mechanisms, influences, limitations and the countermeasures. Chemosphere, 252: 126620. DOI：10.1016/j.chemosphere.2020.126620.

Imhoff PT, Gleyzer SN, McBride JF, et al. 1995. Cosolvent-enhanced remediation of residual dense nonaqueous phase liquids: Experimental investigation. Environmental Science and Technology, 29(8): 1966−1976. DOI：10.1021/es00008a014.

Karaoglu AG, Copty NK, Akyol NH, et al. 2019. Experiments and sensitivity coefficients analysis for multiphase flow model calibration of enhanced DNAPL dissolution. Journal of Contaminant Hydrology, 225: 103515. DOI：10.1016/j.jconhyd.2019.103515.

Kaye AJ, Cho J, Basu NB, et al. 2008. Laboratory investigation of flux reduction from Dense Non-Aqueous Phase Liquid (DNAPL) partial source zone remediation by enhanced dissolution. Journal of Contaminant Hydrology, 102(1-2): 17−28. DOI：10.1016/j.jconhyd.2008.01.006.

Khattab IS, Bandarkar F, Fakhree MAA, et al. 2012. Density, viscosity, and surface tension of water ethanol mixtures from 293 to 323K. Korean Journal of Chemical Engineering, 29(6): 812−817. DOI：10.1007/s11814-011-0239-6.

Kokkinaki A, O'Carroll DM, Werth CJ, et al. 2013. An evaluation of Sherwood–Gilland models for NAPL dissolution and their relationship to soil properties. Journal of Contaminant Hydrology, 155: 87−98. DOI：10.1016/j.jconhyd.2013.09.007.

Liang HL, Falta RW. 2008. Modeling field-scale cosolvent flooding for DNAPL source zone remediation. Journal of Contaminant Hydrology, 96(1-4): 1−16. DOI：10.1016/j.jconhyd.2007.09.005.

Liao PH, Chen Z, Wu M, et al. 2016. The quantitative prediction of DNAPL mobilization under different flow velocity using total trapping number. Acta Science Circumstantiae, 36(9): 3266−3272. (in Chinese) DOI：10.13671/j.hjkxxb.2016.0029.

Luciano A, Mancini G, Torretta V, et al. 2018. An empirical model for the evaluation of the dissolution rate from a DNAPL-contaminated area. Environmental Science and Pollution Research, 25(34): 33992−34004. DOI：10.1007/s11356-018-3193-6.

Lunn SRD, Kueper BH. 1997. Removal of pooled dense, nonaqueous phase liquid from saturated porous media using upward gradient alcohol floods. Water Resources Research, 33(10): 2207−2219. DOI：10.1029/97WR01692.

Marble JC, DiFilippo EL, Zhang Z, et al. 2008. Application of a lumped-process mathematical model to dissolution of non-uniformly distributed immiscible liquid in heterogeneous porous media. Journal of Contaminant Hydrology, 100(1-2): 1−10. DOI：10.1016/j.jconhyd.2008.04.003.

Oba BT, Zheng XH, Aborisade MA, et al. 2021. Environmental opportunities and challenges of utilizing unactivated calcium peroxide to treat soils co-contaminated with mixed chlorinated organic compounds. Environmental Pollution, 291: 118239. DOI：10.1016/j.envpol.2021.118239.

Patil P, Jeppu GP, Vasudevan M, et al. 2023. A review on dissolution of multi-component non-aqueous phase liquids: Recent studies, mechanisms and mass transfer limitations. Desalination and Water Treatment, 283: 164−184. DOI：10.5004/dwt.2023.29230.

Powers SE, Abriola LM, Weber WJ. 1994. An experimental investigation of nonaqueous phase liquid dissolution in saturated subsurface systems: Transient mass transfer rates. Water Resources Research, 30(2): 321−332. DOI：10.1029/93WR02923.

Powers SE, Abriola LM, Weber WJ Jr. 1992. An experimental investigation of nonaqueous phase liquid dissolution in saturated subsurface systems: Steady state mass transfer rates. Water Resources Research, 28(10): 2691−2705. DOI：10.1029/92WR00984.

Ramezanzadeh M, Khasi S, Fatemi M, et al. 2020. Remediation of trapped DNAPL enhanced by SDS surfactant and silica nanoparticles in heterogeneous porous media: Experimental data and empirical models. Environmental Science and Pollution Research, 27(3): 2658−2669. DOI：10.1007/s11356-019-07194-4.

Saba T, Illangasekare TH. 2000. Effect of groundwater flow dimensionality on mass transfer from entrapped nonaqueous phase liquid contaminants. Water Resources Research, 36(4): 971−979. DOI：10.1029/1999WR900322.

Schroth MH, Istok JD, Ahearn SJ, et al. 1996. Characterization of miller-similar silica sands for laboratory hydrologic studies. Soil Science Society of America Journal, 60(5): 1331−1339. DOI：10.2136/sssaj1996.03615995006000050007x.

Song MY, Shi XQ, Ma CL, et al. 2022. Upscaling dissolved phase mass flux for complex DNAPL source zones. China Environmental Science, 42(5): 2095−2104. (in Chinese) DOI：10.19674/j.cnki.issn1000-6923.20220130.003.

Stewart LD, Chambon JC, Widdowson MA, et al. 2022. Upscaled modeling of complex DNAPL dissolution. Journal of Contaminant Hydrology, 244: 103920. DOI：10.1016/j.jconhyd.2021.103920.

Tiwari M, Tripathy DB. 2023. Soil contaminants and their removal through surfactant-enhanced soil remediation: A comprehensive review. Sustainability, 15(17): 13161. DOI：10.3390/su151713161.

Wang HT, Xu HX, Guo QZ, et al. 2019. Structure and mass dissolution of DNAPL pollution source area in saturated porous media. China Environmental Science, 39(8): 3474−3483. (in Chinese) DOI：10.19674/j.cnki.issn1000-6923.2019.0413.

Wang ZJ, Yang ZB, Hu R, et al. 2023. Mass transfer during surfactant-enhanced DNAPL remediation: Pore-scale experiments and new correlation. Journal of Hydrology, 621: 129586. DOI：10.1016/j.jhydrol.2023.129586.

Wang ZJ, Yang ZB, Chen YF. 2023. Pore-scale investigation of surfactant-enhanced DNAPL mobilization and solubilization. Chemosphere, 341: 140071. DOI：10.1016/j.chemosphere.2023.140071.

Yaksi K, Demiray Z, Copty NK. 2020. Impact of cosolvents on the interphase mass transfer of NAPLs in porous media. Water Resources Research, 57(8): e2020WR029326. DOI：10.1029/2020WR029326.

Yang PR, Guo HR, Wang Z, et al. 2022. Influence of distribution characteristics of residual DNAPL on mass transfer in porous media under ethanol co-solvent flushing. Journal of Hydrology, 610: 127932. DOI：10.1016/j.jhydrol.2022.127932.

Yuan M, Wang QF, Guo HR, et al. 2025. Enhancing the dissolution of PCE with the mixed cyclodextrin-ethanol solution for aquifer remediation. Journal of Contaminant Hydrology, 274: 104646. DOI：10.1016/j.jconhyd.2025.104646.

Zhang ZH, Brusseau ML. 2004. Nonideal transport of reactive contaminants in heterogeneous porous media: Distributed-domain model incorporating immiscible-liquid dissolution and rate-limited sorption/desorption. Journal of Contaminant Hydrology, 74(1-4): 83−103. DOI：10.1016/j.jconhyd.2004.02.006.

Zhao YX, Sun YH, Sun HH, et al. 2024. Surfactant-based chemical washing to remediate oil-contaminated soil: The state of knowledge. Toxics, 12(9): 648. DOI：10.3390/toxics12090648.